Economic Geology
Vol. 88, 1993, pp. 916–933

Separation Mechanism in the Formation of Proximal and Distal Tin Polymetallic Deposits, Xinlu Ore Field, Southern China—Evidence from Fluid Inclusion Data

GUOXIANG CHI,

Sciences de la Terre-Centre d'Etudes sur les Ressources Minérales, Université du Québec â Chicoutimi, Chicoutimi, Québec, Canada G7H 2B1, and Changsha Institute of Geotectonics, the Chinese Academy of Sciences

JAYANTA GUHA, AND HUAN-ZHANG LU

Sciences de la Terre-Centre d'Etudes sur les Ressources Minérales, Université du Québec â Chicoutimi, Chicoutimi, Québec, Canada G7H 2B1

Abstract

The Xinlu tin polymetallic ore field in Guangxi Zhuang Autonomous Region, southern China is associated with the Mesozoic Guposhan granitic batholith, which intruded pre-Devonian metasedimentary rocks and late Paleozoic sedimentary rocks including large amounts of carbonates. Dikes of intermediate to granitic compositions similar in age to the granites are widespread. Five tin polymetallic deposits occur in the ore field; among them, the Dachong and Liuhe'ao deposits are located at the contact zone between the granitic intrusions and the Devonian sedimentary rocks and are therefore proximal deposits. The Baimianshan and Shimen deposits, classified as distal deposits, are located in the Devonian sedimentary rocks relatively far above the intrusions and are spatially related to dikes and/or fractures. The Muqiaomian deposit is situated in the sedimentary rocks not far from the contact zone, forming a transitional type between proximal and distal deposits. A correlation between the vertical distance from orebodies to intrusion top surface and the depth of emplacement of the intrusions can be established: proximal deposits are found in the northern part of the ore field, where the granites were emplaced at relatively high levels, in contrast to the distal deposits which are found in the southern part of the ore field, where the granites were emplaced at deeper levels. Both proximal and distal deposits are mainly composed of sulfides, with pyrrhotite and sphalerite being the major components coexisting with cassiterite. The localization of the ore deposits does not appear to be controlled by a specific sedimentary bed at the ore field scale, nor can it be attributed to the effect of metal zonation.

Fluid inclusions in cassiterite from proximal and distal ores and in quartz from granites associated with the proximal deposits have been studied. The chemical system of the ore-forming fluids is H_2O-CO_2 (-other gases)-NaCl-$CaCl_2$. The common coexistence of relatively CO_2-rich gas inclusions (X_{CO_2} = 0.07-0.18) and relatively saline liquid inclusions (NaCl + $CaCl_2$ = 17.1-44.5 wt %) in cassiterite indicates that fluid phase separation is probably an important mechanism of ore deposition. Homogenization temperatures of fluid inclusions are similar between proximal and distal deposits: 250° to 450°C for the Baimianshan deposit, 325° to 450°C for the Shimen deposit, and 350° to 475°C for the Liuhe'ao deposit. This indicates a small temperature gradient in the conduits of the ore-forming fluids. Fluid pressures estimated from isochores range from 70 to 546 bars for the ore deposits and from 123 to 2,822 bars for the granite at Liuhe'ao. The thickness of the overburden at the time of mineralization is estimated to be 3,900 m according to stratigraphic data, the corresponding hydrostatic and lithostatic pressures being 382 bars and 1,032 bars, respectively. Thus the fluid pressure data derived from fluid inclusion study indicate that there was probably a high-pressure contrast between the source of the fluids within the intrusions (approximated by lithostatic pressure) and the contact zone and conduits (approximated by hydrostatic pressure).

A model is proposed to explain the separation of proximal and distal deposits in relation to the depth of emplacement of the intrusions. It is shown that the migration capacity and phase separation fields of the ore-forming fluids are associated with the change from a lithostatic pressure system within the intrusions to a hydrostatic pressure system outside the intrusions and in turn are related to the depth of emplacement of the intrusions. Therefore, when the intrusion is emplaced at high levels, mineralization tends to take place near the contact zone, forming proximal deposits, whereas when the intrusion is emplaced at deeper levels, mineralization is more likely to occur some distance from the intrusion, forming distal deposits.

0361-0128/93/1463/916-18$4.00

Introduction

A PRELIMINARY survey of the literature on tin and other intrusion-associated hydrothermal ore deposits reveals that the distance between the deposits and associated intrusions appears to have a proportional correlation with the depth of emplacement of the intrusions (Chi et al., 1991). Ore deposits occur at or near the contact zone when the intrusion is emplaced at high levels (i.e., proximal deposits) but tend to occur relatively far above the intrusion when the latter is more deeply emplaced (i.e., distal deposits).

This distance-depth correlation does not seem to be merely the effect of metal zoning, nor is it determined by nonmagmatic sources of the ore-forming components. Local depositional conditions, such as a favorable lithologic unit, vary according to specific geologic settings and are not necessarily related to the depth of emplacement of intrusions. Therefore, other factors which are related to the depth of emplacement of intrusions and play a role in localizing ores need to be considered. As the contact zone between the intrusions and the country rocks represents a potential trap for ore-forming components (Kwak, 1987) and is the first favorable depositional site encountered by the ore-forming components issuing from the intrusions, the spatial separation of proximal and distal deposits is actually determined by the capacity of the contact zone to trap ore-forming components versus the capacity of the ore-forming fluids to migrate through the contact zone and carry the ore-forming components to be deposited at a distal site. How the depth of emplacement of intrusions controls the trapping capacity of the contact zone and the migrational capacity of the ore-forming fluids constitutes the main objective of this study.

This paper presents examples from the Xinlu tin polymetallic ore field, Guangxi Zhuang Autonomous Region, southern China, where both proximal and distal deposits are present, and the correlation between ore localization and depth of emplacement of intrusions is well represented. Supported by geologic observations, a preliminary fluid inclusion study was carried out to evaluate the temperature, pressure, composition, and phase evolution of the ore-forming fluids in relation to the depth of emplacement of the intrusions.

Geologic Setting

The Xinlu tin polymetallic ore field is located in eastern Guangxi, southern China (Fig. 1). It is an important part of the Ping-Gui tin polymetallic mineralization district, which is one of the major tin ore-producing districts in southern China. The Xinlu ore field is situated at the southern margin of the Mesozoic Guposhan granitic batholith, which intruded pre-Devonian metasedimentary rocks and late Paleozoic sedimentary rocks including large amounts of carbonates, and is one of the four tin polymetallic ore fields surrounding this batholith (Keda, Wanggao, Shuiyanba, and Xinlu, see insert of Fig. 1).

The Guposhan batholith is a composite intrusion comprising three intrusive phases (see insert of Fig. 1). The first phase of intrusion occupies about three-quarters of the area of the batholith and comprises three zoning parts: the central part (marked by Ic in Fig. 1) of medium- to fine-grained porphyritic hornblende biotite granite; the transitional part (It) of medium- to coarse-grained biotite granite, and the marginal part (Im) of coarse-grained biotite granite. A large number of dark enclaves of intermediate composition with microlitic and porphyritic texture occur in the central part (Ic). The second phase of intrusion (II) cuts the first phase, occupies about one-quarter of the area of the batholith, and is composed of medium- to fine-grained porphyritic biotite granite. The third phase of intrusion (III) comprises small stocks scattered in the first and second phases of intrusion, as well as in the country rocks surrounding the batholith. It is composed of fine-grained or fine-grained porphyritic biotite granite. Rb/Sr whole-rock dating indicates an isochron age of 148.24 Ma for the first phase of intrusion, with an $^{87}Sr/^{86}Sr$ initial ratio of 0.7088 ($n = 12$, $r = 0.998$), and 148.16 Ma for the second phase of intrusion, with an $^{87}Sr/^{86}Sr$ initial ratio of 0.7211 ($n = 13$, $r = 0.995$; Chi, 1992, calculated from the data from Zhang et al., 1985; Pu, 1986; and Xiong, 1986; $\lambda^{87}Rb = 1.42 \cdot 10^{-11}/yr$). No Rb/Sr whole-rock isochron age has been obtained for the third phase of intrusion, but a K/Ar age (whole rock) of 120 Ma has been reported for a third-phase intrusion in Xinlu (You, 1990).

In a normative quartz-alkali feldspar-plagioclase diagram, most samples of the third and second phases of intrusion, and the transitional and marginal parts of the first phase of intrusion, plot on the domains of granite and alkali feldspar granite, whereas the samples from the central part of the first-phase intrusion plot on the domains of granite and adamellite (Chi, 1992). A comparison of the geologic data of the granites of the Guposhan batholith with the criteria distinguishing I- and S-type granites indicates that phase II and III granites belong to S-type granites, whereas phase I granites lie between I- and S-type, but are closer to I-type granites (Chi, 1992).

The geochemical data of different phases of the Guposhan batholith, including major elements, trace elements, and element ratios, have been compared to various criteria distinguishing tin-generating granites from barren granites proposed by different authors (Table 1). It is shown that the proportion of criteria falling in the range of Sn-generating granites in-

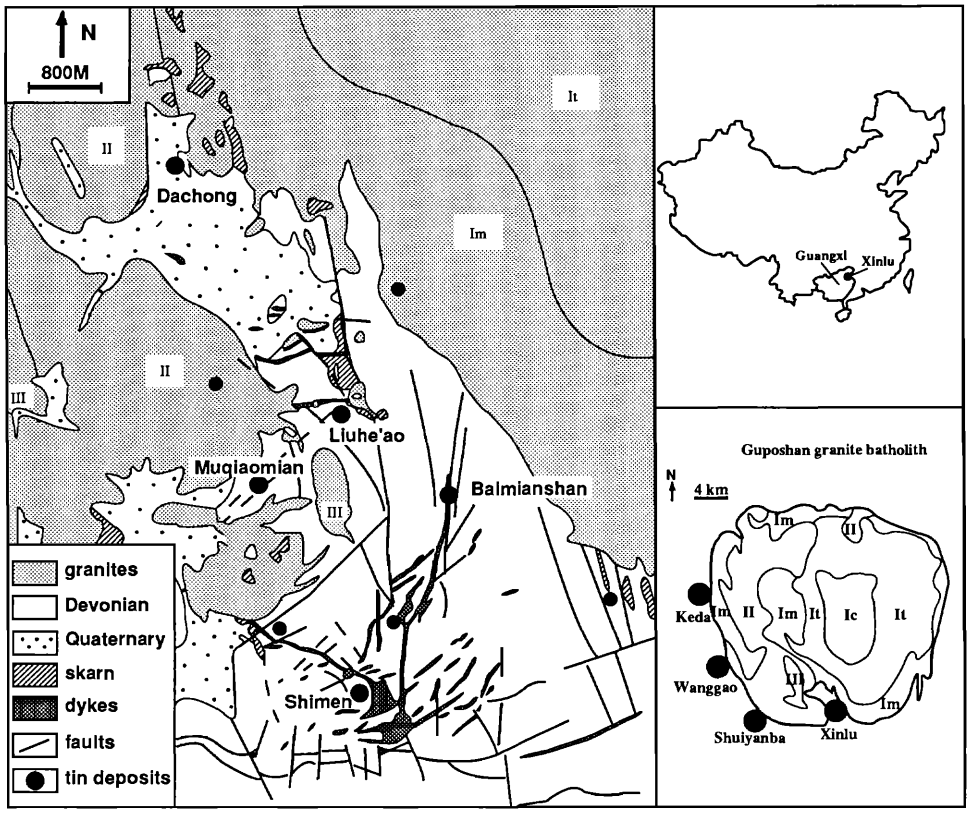

FIG. 1. Geologic map of the Xinlu ore field (modified from Ping-Gui Mining Bureau, unpub. map, 1986) and its position in relation to the Guposhan granite batholith, Guangxi, China. Ic = central part of phase I intrusion, Im = marginal part of phase I intrusion, It = transitional part of phase I intrusion, II = phase II intrusion, and III = phase III intrusion.

creases from the central part through the transitional and the marginal parts of the first-phase intrusion to the second and third phases of intrusion, whereas the proportion of criteria falling in the range of barren granites indicates an opposite trend. It is postulated that tin polymetallic mineralization in the Xinlu ore field is related to the last-phase intrusion of granite, as is the case for most granite-related tin mineralizations.

The Xinlu ore field is surrounded by granites on three sides and is underlain by unexposed granites (Fig. 1). The depth of the top surface of the unexposed granites increases from the northern to the southern part of the ore field (Fig. 2). The granites exposed on the eastern side of the ore field belong to the marginal part of the first-phase intrusion of the Guposhan batholith, those exposed on the western side of the ore field belong to the second-phase intrusion of the batholith. Some small granite stocks belonging to the third-phase intrusion of the batholith are exposed in the central part of the ore field.

Small dikes (1-2 m wide) are widespread throughout the Xinlu ore field (Fig. 1). They are controlled by fractures in the sedimentary rocks. Most of the dikes are intermediate to acidic in composition and generally have a porphyritic texture. Oscillatory zoning is developed in phenocrysts of plagioclase. Abundant titanite and needlelike apatite occur in intermediate dikes, many of which contain carbonate and argillaceous fragments. In a normative Qz-Af-Pl diagram, the samples plot on a wide range of areas: granite, adamellite, granodiorite, quartz monzonite, and quartz monzodiorite (Chi, 1992). The relationship between dikes and granites is not observed, except in one case in the central part of the ore field where an intermediate dike is crosscut by the third-phase granite intrusion. Whole-rock K-Ar ages of three dikes have been analyzed (Chi, 1992): (1) granitic composition, 96 Ma, (2) adamellite composition, 139 Ma, and (3) quartz monzonite composition, 155 Ma (constants adopted: $^{40}K = 1.193 \cdot 10^{-4} \cdot K$; $\lambda e = 0.581 \cdot 10^{-10}/yr$; $\lambda\beta = 4.962 \cdot 10^{-10}/yr$). The orientation of dikes is clearly associated with the geometry of the granitic intrusions. On a regional scale, the dikes in the country rocks surrounding the Guposhan batholith are radially distributed around the batho-

TABLE 1. Geochemical Characteristics of Different Phases of Intrusions of the Guposhan Granite Batholith and Comparison with Criteria Distinguishing Sn-Generating and Barren Granites

Parameters	Phase III	Phase II	Phase Im	Phase It	Phase Ic	Proposed distinguishing criteria: Sn-generating granites	Proposed distinguishing criteria: Barren granites	References
Major elements (wt %)								
SiO_2	75.70 (25)	75.2 (20)	75.33 (15)	73.97 (10)	69.75 (218)	73.38 ± 1.39	70.84 ± 1.41	Tischendorf (1977)
TiO_2	0.07 (25)	0.23 (20)	0.14 (15)	0.16 (10)	0.42 (18)	0.16 ± 0.10	0.34 ± 0.08	
Al_2O_3	12.24 (25)	12.47 (20)	11.96 (15)	13.1 (10)	13.87 (18)	13.97 ± 1.07	14.33 ± 0.23	
Fe_2O_3	0.46 (25)	0.62 (20)	0.79 (15)	1.07 (10)	0.96 (18)	0.80 ± 0.47	1.31 ± 0.29	
FeO	1.37 (25)	1.56 (20)	1.84 (15)	1.81 (10)	2.72 (18)	1.10 ± 0.47	1.78 ± 0.38	
MgO	0.12 (25)	0.24 (20)	0.38 (15)	0.30 (10)	0.97 (18)	0.47 ± 0.56	0.81 ± 0.23	
CaO	0.57 (25)	0.97 (20)	0.82 (15)	1.15 (10)	1.90 (18)	0.75 ± 0.41	1.89 ± 0.40	
Na_2O	3.22 (25)	2.78 (20)	3.29 (15)	3.32 (10)	3.68 (18)	3.20 ± 0.61	3.44 ± 0.32	
K_2O	4.66 (25)	4.46 (20)	4.90 (15)	4.57 (10)	4.33 (18)	4.69 ± 0.68	4.34 ± 0.52	
Trace elements (ppm)								
Sn	27.5 (29)	29.5 (11)	33.3 (4)	8.6 (2)	10.1 (3)	30 ± 15	1–8	
F	1,827 (29)	2,339 (11)	1,433 (4)	1,840 (2)	1,400 (2)	3,700 ± 1,500	250–1,500	
Li	62.3 (26)	38.9 (10)	63 (1)	54 (1)		220 ± 100	31–150	
Rb	557 (28)	432 (11)	420 (3)	356 (2)	296 (2)	550 ± 200	130–300	
Be	12.7 (15)	7 (6)	10 (1)			13 ± 6	2.6–8	
Element ratio								
K/Rb	69.44	85.47	97.09	106.38	121.95	20–100	100–300	Tischendorf et al. (1972)
TiO_2/Ta	43.98	175.76	251.79	301.89	800.00	0.94–71.6	57–4,896	Biossavy-Vinau and Roger (1980)
Mg/Li	11.49	37.04	35.71	28.57		75 ± 30	270 ± 80	Beus and Sitnin (1968)
Rb/Sr	14.93	7.67	17.00	4.68	2.15	>4	<4	Lawrence (1975)
Others								
DI	93.2 (29)	89.9 (20)	91.2 (15)	89.1 (10)	83 (18)	90.06	83.64	Calculated from Tischendorf (1977)
Cm	1.04 (29)	1.58 (20)	0.49 (15)	1.13 (10)	0.58 (18)	2.30	0.54	

The number of samples is given in parentheses
Abbreviations: DI = differentiation index, Cm = corundum

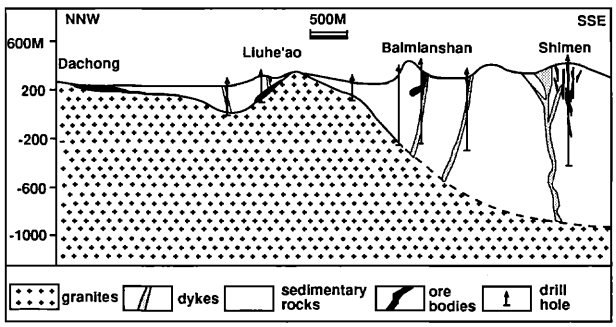

FIG. 2. A north-northwest–south-southeast schematic geologic section across the middle of the Xinlu ore field. The numbers on the vertical scale refer to sea level. The sizes of orebodies and dikes are enlarged because of the small scale of the diagram. Not all drill holes are shown for clarity.

lith; in the Xinlu ore field, the orientation of dikes is affected by the local geometry of granitic intrusions, with dikes in the central part of the ore field trending east-west and those in the southern part of the ore field trending north-south to northeast (Fig. 1). It was postulated that the dikes were formed corresponding to different phases of granite intrusions, with the magmas of the dikes derived from granitic magmas contaminated by sedimentary rocks (Chi, 1992).

The sedimentary rocks in the ore field are mainly Devonian (D) carbonate and clastic rocks, including (from upper to lower) the Rongxian Formation (D_{3r}), the Guilin Formation (D_{3g}), the Donggangling Formation (D_{2d}), the Yujiang Formation (D_{2y}), and the Nagaoling Formation (D_{1n}). D_{3r}, D_{3g}, and D_{2d} are mainly carbonate rocks, and D_{2y} and D_{1n} are mainly sandstone and shales. These sedimentary rocks were folded and fractured during the Indo-Sinian (late Tertiary) and Yanshanian (Jurassic to Cretaceous) orogenies.

Ore Deposit Geology

There are five tin polymetallic deposits in the Xinlu ore field: Dachong, Liuhe'ao, Muqiaomian, Baimianshan, and Shimen (Fig. 1).

The Dachong deposit is located at the northern edge of the ore field (Fig. 1), where the top of the intrusion is about 200 to 250 m above sea level, and most of the sedimentary rocks that lay above the deposit have been eroded. The deposit is located at the contact zone between the granite intrusion and the country rocks and is therefore a proximal deposit. Early-stage skarns and hornfels were formed in the contact zone following intrusion of granite. The skarns are composed mainly of diopside, hedenbergite, andradite, and vesuvianite. Mineralization, in the form of veins and stockworks, consists of magnetite, scheelite, cassiterite, and sulfides (pyrrhotite, sphalerite, pyrite, arsenopyrite, chalcopyrite, and galena) and is superimposed on the skarns and hornfels. Gangue minerals associated with the mineralization include actinolite, epidote, fluorite, plagioclase, mica, calcite, and quartz. The average grade of Sn in the ores is 0.114 to 0.269 percent. Much of the ore cannot be used because a considerable proportion of tin is contained in garnet. Electron microprobe analyses indicate Sn contents of 0.3 to 1.6 wt percent in andradite (Lai and Zen, 1985).

The Liuhe'ao deposit is located in the central northern part of the ore field (Fig. 1), where the top of the intrusion is mainly between 150 and 250 m above sea level, and is covered by Devonian carbonate rocks. A K-Ar age (whole rock) of 120 Ma has been reported for the granite (You, 1990). Some intermediate dikes occur in fractures in the sedimentary rocks and are crosscut by the granite intrusion at the contact zone. Two major proximal orebodies occur at the contact zone. A few small orebodies occur in the sedimentary rocks of the Donggangling Formation (D_{2d}) within about 100 m of the contact zone. The biggest orebody (orebody I) in the contact zone has a strike length of 200 m, a dip length of 160 m, and a thickness of 3 to 14 m. The grade of Sn in the ores varies considerably, with a maximum of 14.5 percent. The orebody is superimposed on the early-stage skarns and hornfels and is composed of cassiterite-bearing massive sulfide ores. Mineral assemblage of the ores is similar to that of the Dachong deposit. Ore minerals include magnetite, scheelite, cassiterite, pyrrhotite, sphalerite, pyrite, arsenopyrite, and chalcopyrite. Gangue minerals include actinolite, chlorite, epidote, fluorite, plagioclase, mica, calcite, and quartz. Wrigglite skarn composed of rhythmic layers of opaque minerals and fluorite, which is typical of Sn skarn (Kwak, 1987), occurs near the orebody.

The Muqiaomian deposit is situated in the west of the ore field (Fig. 1), where the granite intrusion is covered by the marble of the Rongxian Formation (D_{3r}). The top of the intrusion is mainly between 50 and 150 m above sea level. A bed of skarn of about 1 to 6 m thick is developed between the marble and the unexposed granite. Mineralization in the skarn is scattered and economically insignificant. Six steeply dipping orebodies, all controlled by fractures, are found in the marble above the unexposed granite. The strike length of the orebodies is from several tens of meters to 400 m, the dip length varies from 70 to 300 m, and the thickness of the orebodies is between 0.3 to 0.9 m. The orebodies are composed of cassiterite-bearing massive sulfide ores. Ore minerals include cassiterite, pyrrhotite, sphalerite, pyrite, arsenopyrite, and chalcopyrite. Gangue minerals include diopside, calcite, quartz, and fluorite.

The Baimianshan deposit is located in the central south part of the ore field (Fig. 1). Granite in this area is deeply buried under the sedimentary rocks of the Donggangling Formation (D_{2d}), the Yujiang Forma-

tion (D_{2y}), and the Nagaoling Formation (D_{ln}). The unexposed granite body has been encountered by drilling very near the deposit. The top of the intrusion is estimated at about 350 to 250 m below sea level, much deeper than in the Dachong and Liuhe'ao deposits (Fig. 2). Skarns are poorly developed at the contact zone and are economically insignificant. An intermediate dike occurs in a north-south-trending fault (F_2 fault) in the sedimentary rocks. The dike probably extends downward to the granite intrusion surface, but the relationship between the dike and the granite has not been observed. Mineralization is localized in the sedimentary rocks of the Donggangling Formation (D_{2d}) and the Yujiang Formation (D_{2y}), about 500 m above the unexposed granite intrusion. There are three major orebodies: 25, I, and II. Orebody 25 occurs in the Donggangling Formation (D_{2d}). It is controlled by the F_2 fault and is adjacent to an intermediate dike. It is a steeply dipping vein, with a strike length of 330 m, a dip length of 60 m, and a thickness of 0.85 to 17.4 (avg 9.66) m. Orebody II occurs in the top of the Yujiang Formation (D_{2y}), about 30 m below orebody 25. It is a subhorizontal strata-bound orebody, with a discontinuous strike length of 920 m, a dip length of 7 to 127 (avg 67) m, and a thickness of 0.42 to 15.69 (avg 3.6) m. Orebody I is also a subhorizontal strata-bound orebody. It is parallel to, and 5 to 10 m below, orebody II. It has a discontinuous strike length of 800 m, a dip length of 36 to 190 (avg 113) m, and a thickness of 0.33 to 6.16 (avg 2.41) m. The average grade of Sn is 0.57 percent in orebody 25, 0.36 percent in orebody II, and 0.20 percent in orebody I. The orebodies are composed of cassiterite-bearing massive sulfide ores. Metallic minerals include cassiterite, pyrrhotite, sphalerite, pyrite, arsenopyrite, chalcopyrite, galena, jamesonite, and scheelite. Gangue minerals include diopside, wollastonite, actinolite, tremolite, chlorite, epidote, fluorite, sericite, calcite, and quartz. The principal host rocks of the orebodies are marble and limestone. Wall-rock alteration is relatively weak and restricted. Alteration minerals include quartz, sericite, tremolite, chlorite, and epidote.

The Shimen deposit is in the south part of the ore field (Fig. 1). The area is covered by carbonate rocks of the Rongxian Formation (D_{3r}). The unexposed granite was not encountered during drilling (the deepest drill hole in the area is shown in Fig. 2). Dikes of various compositions (from intermediate to acid) are abundant in the area. Mineralization is localized in the marble of the Rongxian Formation (D_{3r}) and is far above the unexposed granite. There are about 30 orebodies, occurring as steeply dipping veins. The orebodies are controlled by fractures and are spatially close to, although not directly hosted by, the dikes. The sizes of the orebodies are relatively small, with strike lengths from 10 to 60 m, dip lengths from 50 to 300 m, and thicknesses from 0.3 to 1 m. The average grade of Sn is 0.85 percent. The orebodies are composed of cassiterite-bearing massive sulfide ores. Metallic minerals include cassiterite, pyrrhotite, sphalerite, pyrite, arsenopyrite, chalcopyrite, galena, and jamesonite. Gangue minerals include diopside, fluorite, calcite, and quartz.

Among the five deposits, the Dachong and Liuhe'ao deposits are proximal, the Baimianshan and Shimen deposits are distal, and the Muqiaomian deposit is a transitional type. The proximal orebodies are superimposed on preore skarns and hornfels in the contact zone. The distal orebodies are located in fractures in the sedimentary rocks and do not appear to be controlled by specific sedimentary beds at the ore field scale. Many of them are closely related to intermediate dikes. Structures which controlled the dike intrusion were probably used as effective conduits by the ore-forming fluid. The process of dike intrusion may have made the structures controlling dike emplacement more permeable and more likely to channelize the fluids from the granites. A correlation between the vertical distance from the orebodies to the intrusion surface and the depth of emplacement of the intrusions is observed: proximal deposits are developed in the northern part of the ore field, where the granites were emplaced at relatively high levels, whereas distal deposits are developed in the southern part of the ore field, where the granites were more deeply emplaced (Fig. 2). The Muqiaomian deposit is not projected in Figure 2, but the fact that the depth of intrusion top surface at Muqiaomian (50-150 m above sea level) is between that at Liuhe'ao (150-250 m above sea level) and that at Baimianshan (350-250 m below sea level) is consistent with its transitional characteristics between proximal and distal types.

Fluid Inclusion Data

Fluid inclusion studies were carried out on proximal (Liuhe'ao) and distal deposits (Baimianshan and Shimen), as well as on granite near the proximal deposit (Liuhe'ao). This work includes fluid inclusion petrography and microthermometry using a U.S.G.S. gas-flow heating-freezing stage and a Chaixmeca stage. Both stages have been calibrated using synthetic fluid inclusions. A few samples were analyzed for gas composition of fluid inclusions using solid microprobe mass spectrometry (Guha et al., 1990).

Occurrence of fluid inclusions

Cassiterite was chosen as the host mineral of fluid inclusions for study for samples of ores from the Liuhe'ao (24 and 25), Baimianshan (XQ132), and Shimen (28) deposits. Fluid inclusions in quartz were examined for samples of granite from Liuhe'ao (CX072, CX071, and CX004). The occurrence of fluid inclusions in cassiterite is complex. In most

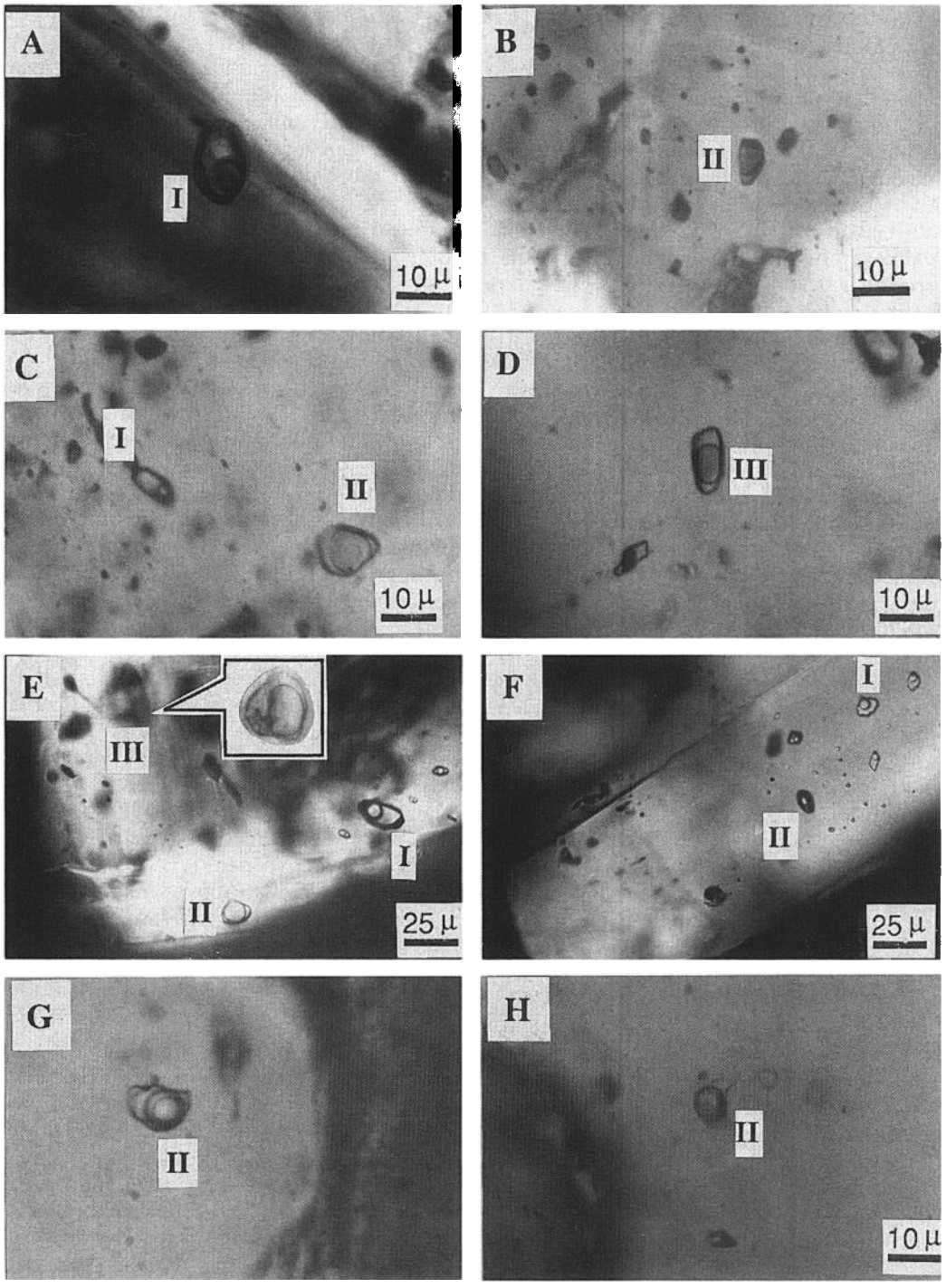

FIG. 3. Photomicrographs of fluid inclusions in cassiterite and quartz. A. Type I fluid inclusion in cassiterite from the Liuhe'ao deposit. B. Type II fluid inclusion in cassiterite from the Liuhe'ao deposit. C. Type I and II fluid inclusions in cassiterite from the Baimianshan deposit. D. Type III fluid inclusion, which homogenizes by critical behavior, in cassiterite from the Baimianshan deposit. E. Type I, II, and III fluid inclusions in cassiterite from the Shimen deposit. F. Group of type I and II fluid inclusions coexisting along growth zones of a cassiterite from the Shimen deposit. G. Type II fluid inclusions showing three phases (aqueous phase, liquid CO_2, and vapor CO_2) at room temperature in quartz of granite from Liuhe'ao. H. Type II fluid inclusion in quartz of granite from Liuhe'ao.

cases fluid inclusions are randomly distributed. In some cases fluid inclusions were observed along growth zones as defined by color zoning. Some fluid inclusions, especially large ones, are isolated. These fluid inclusions are considered to be primary, representing the ore-forming fluids entrapped at the time of cassiterite crystallization. Some fluid inclusions are linearly distributed along healed fractures and are apparently secondary in origin. This study focuses on primary fluid inclusions, and only large (usually >10 μ) fluid inclusions were used in microthermometric measurement. None of the apparent secondary inclusions were used. In granitic quartz, most fluid inclusions appear to be secondary in origin. Some isolated fluid inclusions may be primary. These inclusions, although exhibiting complex interrelationships, represent the fluids that existed in the intrusion after solidification of the magma. Melt inclusions have been observed in a few cases. A group of tiny fluid inclusions usually surrounds the melt inclusions. In some cases these fluid inclusions are distributed in arrays which radiate from the melt inclusion, probably indicating that they were derived from the melt inclusion during crystallization.

Types of fluid inclusions and microthermometry

The fluid inclusions are divided into three types based on microthermometric data. Type I fluid inclusions contain an aqueous phase and a bubble, with or without a halite crystal, at room temperature (Fig. 3A, C, E, and F). The inclusion homogenizes by vapor disappearance. The fluid belongs to the H_2O-NaCl-$CaCl_2$ system. Type II fluid inclusions contain an aqueous phase and a bubble, with or without liquid CO_2, at room temperature (Fig. 3B, C, E, F, G, and H). The inclusion homogenizes by disappearance of the aqueous phase. The fluid belongs to the H_2O-CO_2 (-other gases) system, with a minor quantity of salts. Type III fluid inclusions contain an aqueous phase and a bubble, with or without liquid CO_2, at room temperature (Fig. 3D and E). The inclusion homogenizes by disappearance of the vapor phase or by fading of the meniscus between liquid and vapor (critical). The fluid belongs to the H_2O-CO_2 (-other gases)-NaCl-$CaCl_2$ system. Volume fraction of the bubble at room temperature (or at temperatures above the homogenization temperature of liquid CO_2 and vapor CO_2) is 0.2 to 0.4 for type I, 0.7 to 0.85 for type II, and 0.4 to 0.7 for type III fluid inclusions.

The association of the three types of fluid inclusions varies from one ore type to another. In proximal ores, type I and II fluid inclusions are present, but type I fluid inclusions are more abundant than type II. No type III fluid inclusions were observed. Both types have similar ranges of homogenization temperatures (Fig. 4). They can occur in the same cassiterite crystal in very close proximity. In distal ores, type I, II, and III fluid inclusions are present. They can coexist in the same cassiterite crystal (Fig. 3C, E, and F) and have the same range of homogenization temperatures (Fig. 4). Some type I and II inclusions were observed in the same growth zone of a cassiterite crystal (Fig. 3F). In granite from Liuhe'ao, type I, II, and III fluid inclusions are present.

The microthermometric data of the three types of fluid inclusions are listed in Table 2. Their major features are described as follows.

Type I fluid inclusions: This type of fluid inclusion can be divided into two subtypes: halite-bearing and halite-free (at room temperature) fluid inclusions. Halite-bearing fluid inclusions are mainly found in the proximal deposit at Liuhe'ao. Halite-free fluid inclusions occur in all the deposits and in granite. They all show first melting temperature (T_e) of the aqueous phase below −52°C (mainly between −53° and −60°C), indicating the existence of other bivalent cations in addition to Na^+. For halite-bearing fluid inclusions, the second melting phase is ice, and the last melting phase is halite. The melting temperature of hydrohalite is difficult to determine. The melting temperature of ice is between −20.8° and −42.1°C (mainly between −27° and −35°C). The

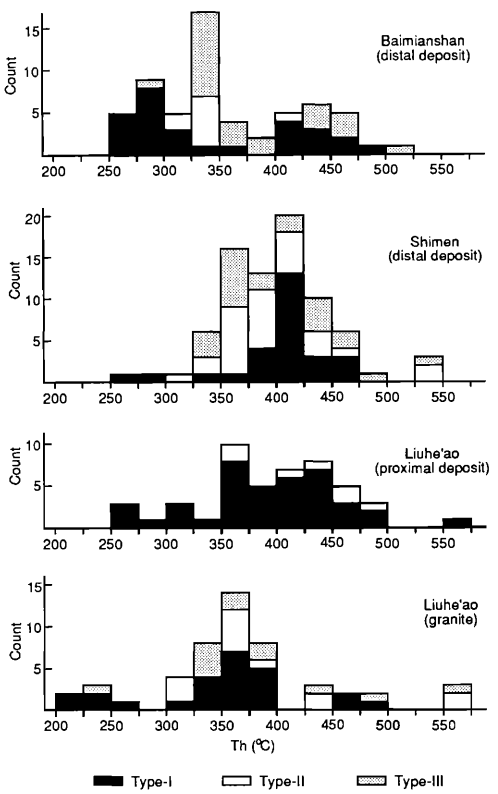

FIG. 4. Histograms of homogenization temperatures of fluid inclusions in cassiterite from proximal and distal deposits and in quartz from granite associated with the proximal deposit.

TABLE 2. Microthermometric Data of Fluid Inclusions from Ore Deposits and Granite

Sample no.	Locality	Host mineral	Type	Size (μ)	Vol % of vapor at 30°C	T_e (°C)	$T_{m_{NaCl\text{-}2H_2O}}$ (°C)	$T_{m_{H_2O}}$ (°C)	$T_{m_{CO_2}}$ (°C)	$T_{h_{CO_2}}$ (°C)	$T_{m_{Clathrate}}$ (°C)	$T_{m_{NaCl}}$ (°C)	T_h (°C)	Salinity of aqueous phase (wt %)[1]	Mole fraction of CO_2	Bulk density (g/cm^3)	Pressure at total T_h (bars)[2]
24	Liuhe'ao (proximal deposit)	Cassiterite	I	18	30	−57.3		−27.9				127.2	429.5 L	31.0		0.87	359
			I	10	30	−59.8		−30.1				313.0	358.6 L	44.5		1.10	175
			I	9	40	−56.6	−32.3	−20.2					431.2 L	22.4		0.80	365
			I	12	25	−56.4		−28.5				182.8	352.0 L	34.3		1.00	162
			II	10	85				−56.4	−33.6 V			433.3 V		0.07	0.18	316
			II	8	80				−56.4	−17.6 V			370.2 V		0.08	0.24	401
25	Liuhe'ao (proximal deposit)	Cassiterite	I	15	25	−59.8	−29.0	−19.2					427.4 L	22.2		0.80	352
			I	8	25	−57.0		−30.4				285.2	425.7 L	42.0		1.00	348
			I	13	30	−58.8		−29.2				313.7	398.2 L	44.2		1.05	267
			I	8	30	−57.7		−28.1				290.6	369.4 L	42.2		1.06	196
			I	14	25	−54.3		−35.5				274.5	426.9 L	42.0		1.00	350
			I	16	25	−55.6		−24.0				331.0	415.2 L	43.1		1.02	315
			I	8	20	−56.4		−34.9				70.1	347.3 L	30.2		0.97	152
			I	8	25	−53.6		−30.8				182.4	362.9 L	33.9		0.98	183
			I	15	30	−56.4		−42.1				231.8	353.3 L	39.0		1.04	164
			I	14	30	−57.0	−27.0	−36.0				136.0	392.1 L	33.4		0.95	251
			I	12	35	−56.3		−34.4				162.6	440.0 L	33.8		0.90	395
			I	14	25	−52.5		−29.6				329.0	479.0 L	44.4		0.97	546
			II	16	80				−58.2	8.8 V			400.7 V		0.18	0.30	402
28	Shimem (distal deposit)	Cassiterite	I	16	40	−61.8	−29.7	−15.1					412.9 L	20.5		0.80	308
			I	14	40	−54.1	−28.1	−13.0					410.3 L	14.4		0.71	299
			I	10	40	−57.7	−27.0	−15.2					410.5 L	20.5		0.80	301
			II	11	80				−57.6	−11.5 V	8.8		389.2 V				
			II	13	80				−57.1	−19.3 V	7.8		389.6 V				
			II	12	80				−56.3	−10.3 V			465.2 V		0.10	0.26	457
			III	12	40	−63.1	−28.1	−7.2	−56.6	−14.9 V			405.4 L				
			III	12	30	−51.3		−8.7	−57.0	−22.2 V			438.1 L				
			III	15	30	−62.0		−11.7	−56.2	−35.0 V			457.0 L				
			III	25	50	−64.1	−25.6	−14.3	−58.8	−18.1 V	5.2		366.9 C				
			III	17	50	−58.8	−25.5	−12.0	−56.8	−14.6 V			393.2 C				
			III	9	50	−53.0	−25.9	−8.8	−58.8	1.0 V			366.0 C				
			III	15	50	−53.4	−24.3	−15.2	−59.2		7.1		365.5 C				
			III	13	60				−59.3	−9.5 V	8.1		392.9 C				

XQ132	Baimianshan (distal deposit)	Cassiterite	I	12	30	−58.7	−30.1	−15.5					318.7 L	20.7		0.91	106
			I	13	30	−68.4	−26.4	−10.3					290.2 L	17.1		0.91	70
			II	12	80				−63.1	−19.4 V	14.4		336.0 V				
			II	13	80				−62.6	−15.5 V	14.1		321.6 V				
			II	12	80				−63.1	−32.5 V	12.4		305.6 V				
			II	9	80				−63.4	−6.7 V	14.3		341.2 V				
			III	12	40	−51.8	−23.3	−12.9	−64.0	2.2 V	9.0		312.8 L				
			III	15	40	−54.4	−27.6	−14.6	−62.8		10.3		347.2 L				
			III	11	60				−68.1	−21.4 V	14.9		349.3 C				
			III	8	70				−65.8	−19.6 V	15.1		335.1 C				
			III	9	60				−71.0	−46.1 V	15.6		336.7 C				
			III	12	60				−66.5	−6.3 V	9.0		360.4 C				
			III	9	60				67.8	−23.5 V	15.2		357.0 C				
			III	10	70				−66.7	−36.4 V	16.9		340.0 C				
			III	23	50				−72.6	11.0 V	16.4		334.0 C				
			III	11	70				−66.5	−17.8 V	15.5		353.9 C				
CX072	Liuhe'ao (granite)	Quartz	I	13	35	−54.9	−23.0	−16.6					347.9 L	21.9		0.89	154
			II	11	70				−58.6	28.9 L			364.7 V		0.38	0.74	1670
			III	15	50				−56.9	18.7 V	7.7		382.7 L	4.5	0.07	0.61	2369
CX071	Liuhe'ao (granite)	Quartz	I	9	35	−63.1		−17.3					350.7 L	20.1		0.87	159
			I	12	30	−61.2	−24.6	−17.7					386.3 L	22.7		0.85	236
			II	11	70				−56.3	29.9 L			447.0 V		0.37	0.72	1952
			II	12	85				−57.9	22.7 L			353.2 V		0.63	0.78	1802
			III	11	40				−56.9	24.2 V	0.5		348.2 L	15.0	0.06	0.76	2822
CX004	Liuhe'ao (granite)	Quartz	I	13	25	−53.1	−24.5	−14.7					338.9 L	20.6		0.89	138
			I	13	30	−55.6	−23.9	−14.1					378.9 L	20.2		0.84	219
			I	10	35	−54.8		−20.8				234.0	330.0 L	33.7		1.02	123
			II	12	70				−59.4	13.3 V	8.9		356.5 V	2.2	0.13	0.41	1276
			II	12	70				−57.8	22.3 V	8.1		344.6 V	3.8	0.17	0.46	1281
			II	12	80				−60.7	18.7 L			380.0 V		0.56	0.83	2298
			II	10	80				−60.9	24.8 V			335.2 V		0.28	0.39	586
			II	12	90				−58.0	28.2 L			350.0 V		0.71	0.69	1299
			III	11	50			−18.5	−59.2	29.6 L	5.6		371.2 L	8.1	0.37	0.74	2011

Abbreviations: C = clathrate, L = liquid, and V = vapor

[1] Salinities are estimated by plotting the microthermometric data on the H_2O-NaCl-$CaCl_2$ phase diagram (Wiliams-Jones and Samson, 1990)

[2] Pressures are estimated by using the equations of state of Brown and Lamb provided in the computer program FLINCOR (Brown, 1989)

melting temperature of halite is between 70.1° and 331.0°C. For halite-free fluid inclusions, the second melting phase is hydrohalite, and the last melting phase is ice. The melting temperature of hydrohalite is between −23.0° and −32.3°C. The melting temperature of ice ranges from −10.3° to −20.2°C. These microthermometric data are interpreted to indicate a compositional system of H_2O-NaCl-$CaCl_2$ for the fluid. By plotting these data on the H_2O-NaCl-$CaCl_2$ phase diagram of Williams-Jones and Samson (1990; Fig. 5), the composition of the aqueous phase and salinities can be estimated (Tables 2 and 3). Salinities of fluid inclusions from the proximal deposit are higher than those from the distal deposits. The total homogenization temperature of a type I fluid inclusion is mainly between 250° and 500°C (Fig. 4). Bulk densities of the inclusions are estimated by using the equation of state of Brown and Lamb for the H_2O-NaCl system, provided in the computer program FLINCOR (Brown, 1989), and are between 0.71 and 1.10 g/cm^3.

Type II fluid inclusions: This type of fluid inclusion is commonly characterized by detectable CO_2 in the vapor phase and by total homogenization to the vapor phase. The microthermometric features, however, are complex and variable. The melting temperatures of solid CO_2 ($T_{m_{CO_2}}$) range from −56.4° to −58.2°C for fluid inclusions from the Liuhe'ao deposit, −56.3° to −57.6°C for those from the Shimen deposit, −62.6° to −63.4°C for the Baimianshan deposit, and −56.3° to −60.9°C for those from the granite at the Liuhe'ao deposit. Homogenization temperatures of liquid and vapor CO_2 ($T_{h_{CO_2}}$) range from −33.6° to +8.8°C (homogenized to vapor phase) for fluid inclusions from the Liuhe'ao deposit, −19.3° to −10.3°C (homogenized to vapor phase) for those from the Shimen deposit, −32.5° to −6.7°C (homogenized to vapor phase) for those from the Baimianshan deposit, and from 13.3° (homogenized to vapor phase) to 18.7°C (homogenized to liquid phase) for those from the granite. Melting temperatures of clathrate ($T_{m_{clathrate}}$) range from 7.8° to 8.8°C for fluid inclusions from the Shimen deposit, 12.4° to 14.4°C for those from the Baimianshan deposit, and 8.1° to 8.9°C for those from the granite. A $T_{m_{clathrate}} > 10$°C for fluid inclusions from Baimianshan indicates the existence of other gas species in addition to CO_2, probably CH_4 and N_2, which is consistent with a $T_{m_{CO_2}} < -56.6$°C and is confirmed by analysis of the gas composition of fluid inclusions using solid microprobe mass spectrometry (described in the following section). These microthermometric data are interpreted to indicate a compositional system of H_2O-CO_2 (-other gases), with a minor quantity of salts, for the fluid. The total homogenization temperature of type II fluid inclusions is mainly between 300° and 450°C (Fig. 4). Bulk densities and a mole fraction of CO_2 of fluid inclusions are estimated, where applicable, by using the equations of state of Brown and Lamb for the systems of H_2O-CO_2 and H_2O-CO_2-

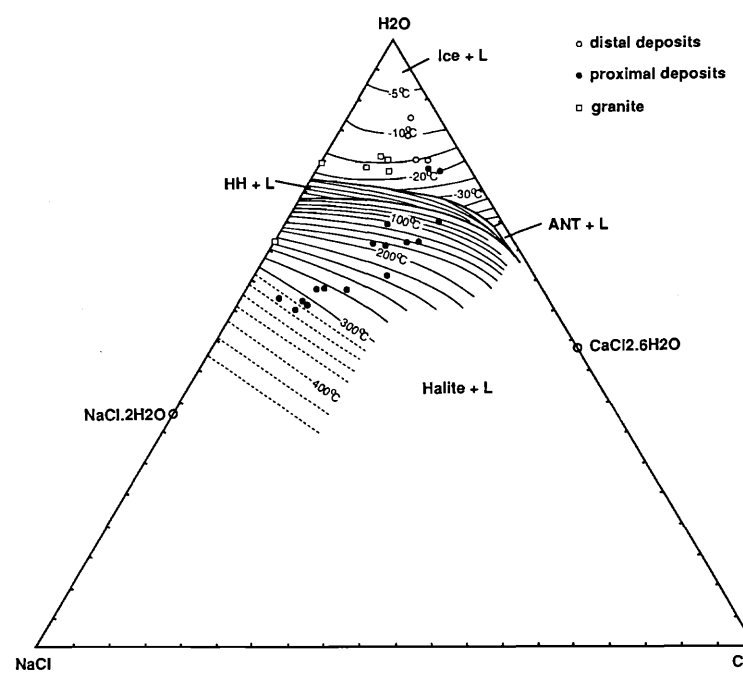

FIG. 5. The composition of the aqueous phase of type I fluid inclusions. Isotherms are from Williams-Jones and Samson (1990).

TABLE 3. Composition of the Aqueous Phase of Type I Fluid Inclusions Estimated from the H_2O-NaCl-$CaCl_2$ Phase Diagram

Sample no.	H_2O (wt %)	NaCl (wt %)	$CaCl_2$ (wt %)
24	69.0	16.5	14.5
	55.5	34.5	10.0
	77.6	4.7	17.7
	65.7	20.0	14.3
25	77.8	6.2	16.0
	58.0	30.5	11.5
	55.8	34.8	9.4
	57.8	32.2	10.0
	58.0	27.5	14.5
	56.9	37.6	5.5
	69.8	8.3	21.9
	66.1	18.2	15.7
	61.0	20.5	18.5
	66.6	13.0	20.4
	66.2	15.5	18.3
	55.6	36.3	8.1
28	79.5	5.5	15.0
	85.6	4.7	9.7
	79.5	7.5	13.0
XQ132	79.3	5.7	15.0
	82.9	6.9	10.2
CX072	78.1	14.7	7.2
CX071	79.9	20.1	0.0
	77.3	12.2	10.5
CX004	79.4	10.9	9.7
	79.8	12.0	8.2
	66.3	33.7	0.0

NaCl, provided in the computer program FLINCOR (Brown, 1989). The mole fraction of CO_2 is between 0.07 and 0.18 for fluid inclusions from the Liuhe'ao deposit, 0.10 for a fluid inclusions from the Shimen deposit, and between 0.13 and 0.71 for fluid inclusions from the granite. The bulk densities are between 0.18 and 0.30 g/cm^3 for fluid inclusions from the ore deposits and between 0.39 and 0.83 g/cm^3 for fluid inclusions from the granite. It is noticed that fluid inclusions from the granite have much higher CO_2 densities and bulk densities than those from the ore deposits.

Type III fluid inclusions: This type of fluid inclusion contains detectable CO_2 in the vapor phase, and the whole inclusion homogenizes to liquid or shows critical homogenization. They were observed in distal deposits and in granite but not in proximal deposits. The microthermometric data of this type of fluid inclusion include first melting temperature of the aqueous phase (T_e), melting temperature of hydrohalite ($T_{m_{NaCl\cdot 2H_2O}}$), melting temperature of ice ($T_{m_{H_2O}}$), melting temperature of solid CO_2 (T_{mCO_2}), homogenization temperature of CO_2 (T_{hCO_2}), melting temperature of clathrate ($T_{m_{clathrate}}$), and total homogenization temperature (T_h). The T_e- and $T_{m_{NaCl\cdot 2H_2O}}$ are similar to those of type I fluid inclusions and indicate the existence of other bivalent cations in addition to Na^+. The $T_{m_{CO_2}}$ ranges from −56.2° to −59.3°C for fluid inclusions from the Shimen deposit, −62.8° to −72.6°C for those from the Baimianshan deposit, and from −56.9° to −59.2°C for fluid inclusions from the granite. The $T_{h_{CO_2}}$ ranges from −35.0° to +1°C (homogenized to vapor phase) for fluid inclusions from the Shimen deposit, −46.1° to +2.2°C (homogenized to vapor phase) for those from the Baimianshan deposit, and 18.7° (homogenized to vapor phase) to 29.6°C (homogenized to liquid phase) for those from the granite. The $T_{m_{clathrate}}$ ranges from 5.2° to 8.1°C for fluid inclusions from the Shimen deposit, 9.0° to 16.9°C for those from the Baimianshan deposit, and from 0.5° to 7.7°C for those from the granite. The total homogenization temperature of type III fluid inclusions is mainly between 325° and 500°C (Fig. 4). These microthermometric data are interpreted to indicate a compositional system of H_2O-CO_2 (-other gases)-NaCl-$CaCl_2$ for the fluid. Despite the relatively complete record of microthermometric data, the composition is difficult to determine for fluid inclusions from the distal deposits because the $T_{h_{CO_2}}$ is invariably lower than the $T_{m_{clathrate}}$, and the $T_{m_{clathrate}}$ is higher than 10°C (Baimianshan). The fluid inclusions from the granite, on the other hand, have $T_{h_{CO_2}} > T_{m_{clathrate}}$, and $T_{m_{clathrate}} < 10$°C and allow estimation of composition and density by approximating the system with H_2O-CO_2-NaCl, using the equation of state of Brown and Lamb, provided in the computer program FLINCOR (Brown, 1989). The mole fraction of CO_2 is between 0.06 and 0.37. Bulk densities are between 0.61 and 0.76 g/cm^3.

In addition to the three types of fluid inclusions, a few melt inclusions were observed within quartz in the granite from Liuhe'ao. They contain silicate minerals and a dark bubble. No phase change was observed in the dark bubble during freezing runs. Some fluid inclusions surrounding the melt inclusions, inferred to be derived from the melt inclusion in the process of crystallization of the melt inclusion, contain a halite crystal or liquid CO_2 at room temperature and homogenize to a liquid or vapor phase, respectively, at elevated temperatures. It is therefore inferred that the initial fluid derived from the granite is probably composed of H_2O, CO_2, and salts.

Gas composition of the fluid inclusions using solid microprobe mass spectrometry

Specific areas without apparent secondary fluid inclusions in cassiterite from a sample from the Liuhe'ao deposit (24) and a sample from the Baimianshan deposit (XQ132) were cut from doubly polished sections for analysis by solid microprobe mass spectrometry. The method of analysis has been described in detail by Guha et al. (1990). The sample was held by the solid probe which was inserted directly into

TABLE 4. Gas Composition of Fluid Inclusions Using Solid Microprobe Mass Spectrometry

Sample no.	CH_4 (mole %)	H_2O (mole %)	N_2 or CO (mole %)	CO_2 (mole %)
24	1.49	75.47	1.61	21.43
XQ132	3.34	75.79	12.95	7.92

the ionization chamber and heated stepwise from 100° to 700°C at a heating rate of 20°C/min. The gas composition of decrepitated fluid inclusions, which is a mixture of different types of fluid inclusions, was detected at different temperatures. The integration of composition from 300° to 600°C, which is the main range of decrepitation of fluid inclusions, gives the bulk gas composition of the mixture of the fluid inclusions. The results are listed in Table 4. They show that fluid inclusions from the Baimianshan deposit contain significantly higher quantities of CH_4 and CO or N_2 than those from the Liuhe'ao deposit, which is consistent with the microthermometric data.

Systematics of fluid temperature and pressure

Homogenization temperatures of fluid inclusions from different occurrences are compared in Figure 4. It can be seen that the temperatures of the ore-forming fluids of the distal deposits are apparently only slightly lower than those of the proximal ones, possibly indicating very small temperature gradients in the hydrothermal systems.

Isochores of some fluid inclusions were calculated using the equations of state of Brown and Lamb (provided in the computer program FLINCOR, Brown, 1989) for the systems of H_2O-NaCl (for type I fluid inclusions), H_2O-CO_2 (for some type II fluid inclusions), and H_2O-CO_2-NaCl (for some type II and III fluid inclusions). The results are illustrated in Figure 6. Many of the microthermometric data, notably those from the Baimianshan deposit as discussed above, cannot be used to calculate isochores because $T_{h_{CO_2}}$ is lower than $T_{m_{clathrate}}$ and/or $T_{m_{clathrate}}$ is higher than 10°C.

Pressures at total homogenization (P_{th}) were calculated and are listed in Table 2. For the Liuhe'ao deposit, P_{th} is between 152 and 546 bars for type I fluid inclusions and is between 316 and 402 bars for type II fluid inclusions. For the Shimen deposit, P_{th} is between 299 and 308 bars for type I fluid inclusions and is 457 bars for a type II fluid inclusion. For the Baimianshan deposit, P_{th} is between 70 and 106 bars for type I fluid inclusions. For the granite, P_{th} is between 123 and 236 bars for type I fluid inclusions, between 586 and 2,298 bars for type II fluid inclusions, and between 2,011 and 2,822 bars for type III fluid inclusions. It is noticed that P_{th} for fluid inclusions from the ore deposits is significantly lower than that for fluid inclusions from the granite. It is also

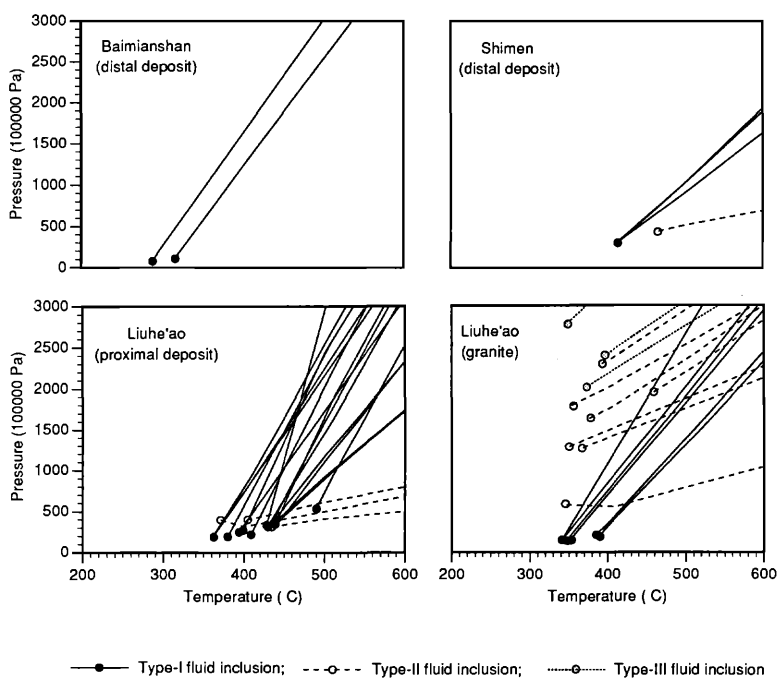

FIG. 6. Isochores of fluid inclusions from the Liuhe'ao, Shimen, and Baimianshan deposits and the granite. The equations of state are from Brown and Lamb (provided in FLINCOR, Brown, 1989) for both H_2O-NaCl and H_2O-CO_2 systems. Circles indicate temperature and pressure at homogenization.

notable that P_{th} calculated from type I fluid inclusions is similar to that calculated from type II fluid inclusions from the ore deposits. As will be discussed in the following section, type I and II fluid inclusions from the ore deposits are interpreted to represent coexisting immiscible fluids. Thus, P_{th} represents the real fluid pressure at the site of mineralization. The error of pressure introduced by using the H_2O-NaCl system to approximate type I fluid inclusions (H_2O-NaCl-$CaCl_2$ system) is small, because the calculated pressure (P_{th}) lies on the liquid-vapor curve (in the temperature-pressure space), which is similar for the H_2O-NaCl and H_2O-$CaCl_2$ systems in the range of homogenization temperatures of this study (see Zhang and Frantz, 1989, fig. 5). For example, the difference of P_{th} values between the H_2O-NaCl and H_2O-$CaCl_2$ systems is <50 bars at T_h = 400°C. The difference of P_{th} values between the H_2O-NaCl and H_2O-NaCl-$CaCl_2$ systems at given homogenization temperatures should be smaller than the P_{th} values between the H_2O-NaCl and H_2O-$CaCl_2$ systems. In fact, Zhang and Frantz (1987, p. 344, eq 10) have used the same liquid-vapor curve for H_2O, H_2O-NaCl, H_2O-KCl, H_2O-$CaCl_2$, and mixing systems (assuming ideal mixing) with various solute concentrations in constructing isochores; thus, for a given homogenization temperature, P_{th} is the same for any of the above compositional systems.

According to the stratigraphic data of the region (Geologic Team 204 of Guangxi, 1986), the maximum thickness of the strata above the deposits is between 2,600 and 3,900 m. Considering the effect of tectonic shortening and thickening caused by the Mesozoic Indo-Sinian movements which predated the mineralization, a thickness of 3,900 m is adopted for the overburden above the level of ore deposits at the time of ore formation. At this depth, the hydrostatic pressure is 382 bars (for a water density of 1 g/cm^3), and the lithostatic pressure is 1,032 bars (for a rock density of 2.7 g/cm^3). Therefore, the above P_{th} data indicate that the pressure of the ore-forming fluids is close to hydrostatic pressure at the site of mineralization. The variation of P_{th} for fluid inclusions from granite between <hydrostatic and >lithostatic may be due to fluctuation of pressure systems in the intrusion. However, these P_{th} data may be the minimum fluid pressure values, because there is no obvious evidence that the fluid in any type of fluid inclusions from the granite is in equilibrium with another immiscible fluid at the time of entrapment. Thus, fluid pressure at entrapment is higher than P_{th}. This is especially important for the type I fluid inclusions, where isochores have very steep slopes (see Fig. 6). On the other hand, it must be pointed out that the pressures estimated from isochores are strongly dependent on the equation of state adopted. The equation of Bowers and Helgeson (also in the computer program FLINCOR, Brown, 1989) generally yields lower pressure values in the temperature range of this study than the equation of Brown and Lamb. For example, the P_{th} of a type III fluid inclusion from granite is 2,011 bars for the equation of Brown and Lamb but is 1,435 bars for the equation of Bowers and Helgeson. Bearing these differences in mind, it is reasonable to postulate that a fluid pressure ≥ lithostatic pressure (but ≤ lithostatic pressure + tensile strength of the confining rocks) was maintained within the intrusion. The pressure which is larger than lithostatic pressure is probably due to the overpressure caused by the exsolution of hydrous liquids from the magma (Burnham, 1979). Therefore, from the fluid inclusion data, it is possible to infer that a fluid pressure contrast existed between the fluids within the intrusion (approximated by lithostatic pressure) and those in the conduits and the contact zone outside the intrusion (approximated by hydrostatic pressure), a situation believed by Cunningham (1978) to exist in a porphyry mineralization system. Heinrich (1990) also suggested that the formation of mesothermal tin (-tungsten) deposits is dominated by fluid processes at the transition from a magmatic lithostatic source regime to a cooler hydrostatic depositional environment.

Fluid phase separation

The common coexistence of relatively CO_2-rich gas inclusions (X_{CO_2} = 0.07–0.18) and relatively saline liquid inclusions (NaCl + $CaCl_2$ = 17.1-44.5 wt %) with similar homogenization temperatures in cassiterite indicates that two immiscible fluids existed at the site of mineralization. These immiscible fluids may have been derived from phase separation of an initial monophase fluid. The initial fluid may belong to an H_2O-CO_2 (-other gases)-NaCl-$CaCl_2$ system, represented by type III fluid inclusions. The immiscible liquid and vapor phases resulting from phase separation belong to an H_2O-NaCl-$CaCl_2$ system and an H_2O-CO_2 (-other gases) minor quantity of salts system, represented by type I and II fluid inclusions, respectively. In proximal deposits, type I fluid inclusions have very high salinities, indicating strong partitioning of salts into the liquid phase. No type III fluid inclusions were entrapped. It is inferred that the position of the fluid at the site of proximal mineralization is probably relatively far from the critical point in the immiscible loop in a P-T coordinate, so the composition of the coexistent liquid and vapor phases is well differentiated, underlining extensive phase separation. Fluctuation of fluid pressure will not shift the position of the fluid outside the immiscible loop, thus no type III fluid inclusions were entrapped. In distal deposits, type I fluid inclusions have moderate salinities, indicating less intensive phase separation than in proximal deposits. Type III fluid inclusions

are abundant, and many of them show critical homogenization. These fluid inclusions may have been entrapped before phase separation, at a slightly higher pressure. It is possible that the properties (especially densities) of the initial fluid were modified during its ascent from the granite intrusion to the site of distal deposits, so that the position of the fluid is probably close to the critical point in the immiscible loop in a P-T coordinate, and the coexistent liquid and vapor phases resulting from phase separation are less differentiated than in proximal deposits. A slight fluctuation of fluid pressure will shift the fluid outside the immiscible loop, thus type III fluid inclusions could be entrapped.

Fluid inclusion evidence for phase separation is recorded from many tin and tungsten deposits (Heinrich and Eadington, 1986). Phase separation has been proven to be a major process responsible for the deposition of a variety of hydrothermal deposits, and cassiterite is one of the minerals which is most likely to deposit from boiling hydrothermal solutions (Drummond and Ohmoto, 1985). This is related to the fact that phase separation results in an exsolution of CO_2 and other gases and an increase in pH values in the liquid phase, and the increase in pH values has been shown by many authors (e.g., Jackson and Helgeson, 1985; Wilson and Eugster, 1990) to be an effective cause of cassiterite deposition. The oxidizing effect due to H_2 loss to the vapor phase may be a more effective mechanism of cassiterite deposition (Heinrich, 1990). It is believed that phase separation is likely a major mechanism of ore deposition for the proximal deposits in Xinlu and may have also played a role in the deposition of the distal deposits. Because cassiterite precipitation is sensitive to phase separation, it is reasonable to assume that ore deposition took place at the same site as, or not far from, the onset of phase separation. The vertical distance of two-phase flow without significant precipitation of cassiterite is considered to be small.

Discussion

From the geologic setting of the Xinlu ore field and the geologic characteristics of the ore deposits, it is inferred that the ore-forming fluids for both proximal and distal deposits were derived mainly from the latest stage granitic intrusions. The separation of proximal and distal deposits does not seem to be caused by nonmagmatic sources of ore-forming components, nor can an effect of metal zonation be established. Most of the distal orebodies are steeply dipping veins and are not controlled by specific sedimentary beds at the ore field scale.

From the fact that the distance between ore deposits and associated intrusions shows a proportional correlation to the depth of emplacement of the intrusions, and from the fluid inclusion data, it is proposed that the process leading to the separation of proximal and distal deposits is related to the depth of emplacement of intrusions. The depth of emplacement of intrusions may influence the localization of ore deposits with respect to the intrusions in two ways: it influences the dynamics of the ore-forming fluids derived from the intrusions, and it influences the level at which phase separation takes place. These two aspects are discussed as follows.

Fluid flow dynamics in relation to the depth of emplacement of intrusions

The fluid inclusion data indicate that the temperatures of the ore-forming fluids of the distal deposits are similar to those in the proximal deposits, despite their difference of several hundred meters in distance from the intrusions. This implies that the ore-forming fluids must have ascended very rapidly. The fluid pressure inferred from fluid inclusions indicates that the fluid pressure at the site of ore deposition is close to hydrostatic pressure, and the pressure of the fluids within the intrusion may be approximated by lithostatic pressure. It is possible that a pressure contrast existed between the conduit system (hydrostatic), which consists of faults, fractures, and dike-controlling structures, and the interior of the intrusion (lithostatic). This pressure contrast is proportional to the depth of emplacement of the intrusion, as illustrated in Figure 7. As the fluid flow rate is proportional to the pressure contrast, it can be seen that the fluid flow rate increases with increasing depth of emplacement of the intrusion.

Three consequences of high fluid flow rate, which are related to transport and deposition of ore components, can be expected. First, a temperature drop of the ore-forming fluid will be minimized, and the ore-forming components can be transported through a longer distance before they are precipitated. Second, the level of effective incorporation of meteoric water (fluid mixing) will be raised, because at the departure

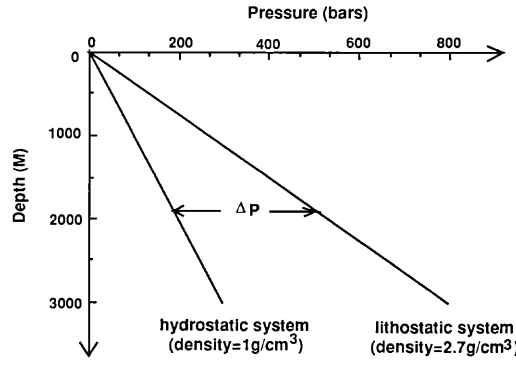

FIG. 7. Depth-pressure diagram showing that the contrast of hydrostatic and lithostatic pressure increases with depth.

of the ore-forming fluid, the fluid flow rate may be so high that the overpressure caused by fluid resistance to upward flow will resist the incorporation of meteoric water; thus effective incorporation of meteoric water will not occur until the ore-forming fluid flows to a higher level and the flow rate slows down, probably because of the development of branches of conduits. Third, effective wall-rock reactions will not take place until the ore-forming fluid flows to shallow levels and the flow rate slows down, because a high flow rate reduces the time of water-rock reactions.

Generally the contrast between lithostatic and hydrostatic pressure will be greater when the intrusion is emplaced at depth and this will enhance the capacity of the ore-forming fluid to migrate farther. The ore-forming elements will be transported to a distance from the intrusion before deposition.

Level of phase separation in relation to the depth of emplacement of intrusions

In addition to fluid dynamics, fluid phase separation, which is an important mechanism of ore deposition in Xinlu as discussed above, is also related to the depth of emplacement of the intrusion. Since phase separation took place at the site of ore deposition, the level of phase separation with respect to the depth of emplacement of intrusions is significant for the localization of proximal versus distal deposits.

Phase separation tends to occur where a sharp drop in pressure exists, which is most likely the case at the contact zone, where there is a fluid pressure contract between the conduit system (hydrostatic) and the interior of the intrusion (lithostatic), as indicated by the fluid inclusion data. However, phase separation may fail to take place at the contact zone if the intrusion is emplaced deeply. It has been noticed by many authors (e.g., Cunningham, 1978) that a sharp drop in fluid pressure in an epizonal environment is more likely to cause extensive boiling than a comparable change in a deeper environment.

Figure 8 shows schematically how the depth of emplacement of the intrusion controls the sites of phase separation with respect to the intrusion. This figure has no quantitative significance except that the topological shape of the phase boundaries resembles that of the H_2O-rich side of the H_2O-CO_2-NaCl system (Gehrig et al., 1979), which is probably the case in the Xinlu ore field. A and C represent the points of departure of the ore-forming fluids near the contact zone of the intrusion. The depth of emplacement of the intrusion is small at A and large at C. In the case of point A, the ore-forming fluid was originally under the lithostatic system and was in the one-phase domain. When the pressure system changes from lithostatic to hydrostatic, point A is in the two-phase area. Therefore, phase separation occurs immediately at the contact zone (point B). In the case of distal deposits, the ore-forming fluid was also originally under the lithostatic system (point C) and was in the one-phase domain. However, when the pressure system changes from lithostatic to hydrostatic, point C is still in the one-phase area. Therefore, the ore-forming fluid can move a certain distance up before reaching the two-phase area of the hydrostatic system (at D). The deeper the fluid originated, the longer distance it had to migrate to reach the two-phase state.

Figure 8 assumes that the composition and density of the fluid do not change during the migration, but the temperature drops slightly. If the composition and density of the ore-forming fluid is changed during the migration (from C to D), the phase boundaries will change correspondingly. This will change the position of the fluid in relation to the phase boundaries. The difference in the extent of phase separation between the proximal and distal deposits in the Xinlu ore field is probably caused by the compositional and density change of the distal ore-forming fluids during the migration.

In summary, the influence of the depth of emplacement of intrusions on phase separation is such that

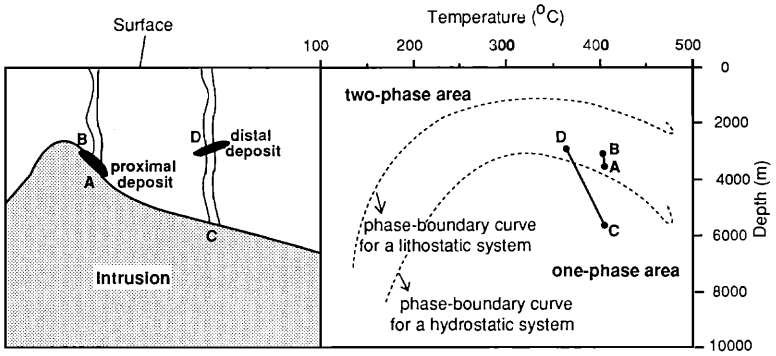

FIG. 8. A schematic model showing how the depth of emplacement of the intrusion controls the sites of phase separation with respect to the intrusion. A-B and C-D represent the flow paths of the ore-forming fluids. For more detailed explanation see text.

the ore-forming fluid issuing from intrusions is more likely to be subject to a phase separation at the contact zone (where there is a sudden pressure drop) when the magmatic intrusion is emplaced at higher levels than when the intrusion is emplaced more deeply. In the former case, a proximal deposit may form as a result of phase separation; in the latter case, the fluid can carry the ore-forming components to a high level to form a distal deposit, where phase separation may or may not occur, depending on the extent of modification of the fluid during its ascent.

Conclusions

The objective of this study was to examine the mechanism of the separation of proximal and distal deposits in the Xinlu ore field. The main conclusions are summarized as follows:

1. The majority of the ore-forming fluids and metals in the Xinlu ore field were derived from latest stage granitic intrusions. The localization of proximal and distal deposits is not controlled by specific lithological units nor can an effect of metal zonation be established.
2. Phase separation is likely a major mechanism of ore deposition for the proximal deposits and may have also played a role in the deposition of the distal deposits.
3. Homogenization temperatures of fluid inclusions are similar between proximal and distal deposits, possibly indicating a small temperature gradient in the hydrothermal systems and a high rate of fluid flow.
4. A pressure contrast may have existed between the interior of the intrusions (approximated by lithostatic pressure) and the contact zone and the fractures in the country rocks (approximated by hydrostatic pressure).
5. The migrational capacity of the ore-forming fluids is related to the depth of emplacement of the intrusions. The pressure contrast between hydrostatic and lithostatic systems rapidly increases with depth, so that the flow rate of ore-forming fluids derived from an intrusion increases with increasing depth of emplacement of the intrusion, the effect of temperature drop is reduced, and the ore-forming components can be transported to a longer distance before being deposited.
6. The phase separation fields of the ore-forming fluids are related to the depth of emplacement of the intrusions such that when the intrusion is emplaced at high levels, the ore-forming fluid released from the intrusion changes from the one-phase domain under a lithostatic system (within the intrusion) to the two-phase domain under a hydrostatic system (at the contact zone), and phase separation takes place at the contact zone; whereas when the intrusion is emplaced at deeper levels, the ore-forming fluid released from the intrusion remains in the one-phase domain after the pressure system has changed from lithostatic (within the intrusion) to hydrostatic (at the contact zone), and phase separation does not take place until the fluid ascends to a higher level.
7. The separation of proximal and distal deposits in the Xinlu ore field is mainly controlled by the depth of emplacement of the intrusions. Proximal deposits were developed when the intrusion was emplaced at relatively high levels, whereas distal deposits were developed when the intrusion was emplaced relatively deeply.

Acknowledgments

The authors would like to thank the Ministère de l'Enseignement Supérieur et des Sciences du Québec (Programme Action Structurante) and the Chinese Academy of Sciences for the scholarships provided to Guoxiang Chi and the Natural Sciences and Engineering Research Council and the Research Foundation of the Université du Québec à Chicoutimi for research grants to Jayanta Guha. Help from the Changsha Institute of Geotectonics and the Ping-Gui Mining Bureau of Guangxi, as well as G.-D. Chen, H.-H. Yin, H.-Y. Hu, G.-Y. Xie, L.-B. Qiu, J.-S. You, Z.-C. Dong, and G.-Y. Huang in the first stage of this work, is gratefully acknowledged. The manuscript also benefited from the critical comments and suggestions of A. E. Williams-Jones of McGill University and two *Economic Geology* reviewers for which the authors are thankful.

December 18, 1991; February 11, 1993

REFERENCES

Beus, A. A., and Sitnin, A. A., 1968, Geochemical specialization of magmatic complexes as criteria for the exploration of hidden deposits: Internat. Geol. Cong., 23rd, Prague, 1968, sec. 6, Proc., p. 101–105.

Boissavy-Vinau, M., and Roger, G., 1980, The TiO_2/Ta ratio as an indicator of the degree of differentiation of tin granites: Mineralium Deposita, v. 15, p. 231–236.

Brown, P. E., 1989, FLINCOR: A microcomputer program for the reduction and investigation of fluid-inclusion data: Am. Mineralogist, v. 74, p. 1390–1393.

Burnham, C. W., 1979, Magmas and hydrothermal fluids, *in* Barnes, H. L., ed., Geochemistry of hydrothermal ore deposits, 2nd ed.; New York, John Wiley and Sons, p. 71–136.

Chi, G.-X., 1992, Polygenetic control of the localization of proximal versus distal deposits in the Xinlu tin polymetallic ore field, Guangxi, southern China: Unpub. Ph.D. thesis, Univ. Quebec, Chicoutimi, 251 p.

Chi, G.-X., Guha, J., and Lu, H.-Z., 1991, Correlating the depth of granitic intrusions with the localization of associated hydrothermal deposits: Examples, preliminary model and possible application to mineral prospecting [abs.]: Geol. Assoc. Canada-Mineralog. Assoc. Canada Program with Abstracts, v. 16, p. A23.

Cunningham, C. G., 1978, Pressure gradients and boiling as mechanisms for localizing ore in porphyry systems: U.S. Geol. Survey Jour. Research, v. 6, p. 745–754.

Drummond, S. E., and Ohmoto, H., 1985, Chemical evolution and mineral deposition in boiling hydrothermal systems: ECON. GEOL., v. 80, p. 126–147.

Gehrig, M., Lentz, H., and Franck, E. U., 1979, Thermodynamic properties of water-carbon dioxide-sodium chloride mixtures at high temperatures and pressures, *in* Timmerhaus, K. D., and Barber, M. S., eds., Physical properties and material synthesis, v. 1: New York, Plenum Press, p. 539–542.

Geologic Team 204 of Guangxi, 1986, Extent of geologic work in the Ping-Gui district and suggestions for further prospecting: Xiwan, Guangxi, Ping-Gui Mining Bur., unpub. rept. (in Chinese).

Guha, J., Lu, H.-Z., and Gagnon, M., 1990, Gas composition of fluid inclusions using solid probe mass spectrometry and its application to study of mineralizing processes: Geochim. et Cosmochim. Acta, v. 54, p. 553–558.

Heinrich, C. A., 1990, The chemistry of hydrothermal tin (-tungsten) ore deposition: ECON. GEOL., v. 85, p. 457–481.

Heinrich, C. A., and Eadington, P. J., 1986, Thermodynamic predictions of the hydrothermal chemistry of arsenic, and their significance for the paragenetic sequence of some cassiterite-arsenopyrite-base metal sulfide deposits: ECON. GEOL., v. 81, p. 511–529.

Jackson, K. J., and Helgeson, H. C., 1985, Chemical and thermodynamic constraints on the hydrothermal transport and deposition of tin: II. Interpretation of phase relations in the southeast Asian tin belt: ECON. GEOL., v. 80, p. 1365–1378.

Kwak, T. A. P., 1987, W-Sn skarn deposits and related metamorphic skarns and granitoids: Devel. Econ. Geology, v. 24, 451 p.

Lai, L.-R., and Zen, N.-S., 1985, Geochemical behaviour of tin in skarn formation, Ping-Gui region, Guangxi: Geology Prospecting, v. 21, p. 16–21 (in Chinese).

Lawrence, G., 1975, The use of rubidium/strontium ratios as a guide to mineralization in the Galway granite, Ireland: Devel. Econ. Geology, v. 1, p. 353–370.

Ping-Gui Mining Bureau, 1986, A brief description of the exploration extent of the ore deposits and occurrences in the Ping-Gui mining district: Xiwan, Guangxi, unpub. map. (in Chinese).

Pu, L.-P., 1986, Origin of the Guposhan granite batholith and the enclaves: Unpub. M.Sc. thesis, Changsha, China, Central-South Univ. Technology. (in Chinese with English abs.).

Tischendorf, G., 1977, Geochemical and petrographic characteristics of silicic magmatic rocks associated with rare-element mineralization, *in* Stemprok, M., Burnol, L., and Tischendorf, G., eds., Metallization associated with acid magmatism: Prague, Czechoslovakia Geol. Survey, v. 2, p. 41–98.

Tischendorf, G., Lachelt, S., Lange, H., Palchen, W., and Meinel, G., 1972, Geochemical specialization of granitoids in the territory of the German Democratic Republic: Internat. Geol. Cong., 24th, Montreal, 1972, sec 4, Proc., p. 266–275.

Williams-Jones, A. E., and Samson, I. M., 1990, Theoretical estimation of halite solubility in the system NaCl-$CaCl_2$-H_2O: Application to fluid inclusions: Canadian Mineralogist, v. 28, p. 299–304.

Wilson, G. A., and Eugster, H. P., 1990, Cassiterite solubility and tin speciation in supercritical chloride solutions, *in* Spencer, R. J., and Chou, I.-M., eds., Fluid-mineral interaction: A tribute to H. P. Eugster: Geochemical Soc. Spec. Pub. 2. p. 179–195.

Xiong, Y.-L., 1986, Classification, evolution and mineralization zoning of the tin deposit at Lantoushan, the Shuiyanba tin ore field, northeast Guangxi: Unpub. M.Sc. thesis, Wuhan, China, Wuhan College Geology, (in Chinese with English abs.).

You, J.-S., 1990, Geologic features of granites and dikes and metallogenesis in the Xinlu tin ore field, He County, Guangxi province: Unpub. M.Sc. thesis, Changsha Inst. Geotectonics, Academia Sinica, 47 p. (in Chinese with English abs.).

Zhang, D.-Q., Wang, X.-Y., and Sun, G.-Y., 1985, Cooling history and emplacement ages of the Guposhan-Lishong granite masses, Guangxi: Geology Review, v. 31, p. 232–239 (in Chinese).

Zhang, Y.-G., and Frantz, J. D., 1987, Determination of the homogenization temperatures and densities of supercritical fluids in the system NaCl-KCl-$CaCl_2$-H_2O using synthetic fluid inclusions: Chem. Geology, v. 64, p. 335–350.

—— 1989, Experimental determination of the compositional limits of immiscibility in the system $CaCl_2$-H_2O-CO_2 at high temperatures and pressures using synthetic fluid inclusions: Chem. Geology, v. 74, p. 289–308.